



HAL
open science

Submicronic Laue diffraction to determine in-depth strain in very closely matched complex HgCdTe/CdZnTe heterostructures with a 10^{-5} resolution

Xavier Biquard, P. Ballet, A. Tuaz, Pierre-Henri Jouneau, F. Rieutord

► To cite this version:

Xavier Biquard, P. Ballet, A. Tuaz, Pierre-Henri Jouneau, F. Rieutord. Submicronic Laue diffraction to determine in-depth strain in very closely matched complex HgCdTe/CdZnTe heterostructures with a 10^{-5} resolution. *Journal of Synchrotron Radiation*, 2021, 28 (1), pp.181 - 187. 10.1107/S1600577520013211 . hal-03025086

HAL Id: hal-03025086

<https://hal.science/hal-03025086>

Submitted on 5 Jan 2021

HAL is a multi-disciplinary open access archive for the deposit and dissemination of scientific research documents, whether they are published or not. The documents may come from teaching and research institutions in France or abroad, or from public or private research centers.

L'archive ouverte pluridisciplinaire **HAL**, est destinée au dépôt et à la diffusion de documents scientifiques de niveau recherche, publiés ou non, émanant des établissements d'enseignement et de recherche français ou étrangers, des laboratoires publics ou privés.



Submicronic Laue diffraction to determine in-depth strain in very closely matched complex HgCdTe/CdZnTe heterostructures with a 10^{-5} resolution

X. Biquard, P. Ballet, A. Tuaz, P. H. Jouneau and F. Rieutord

J. Synchrotron Rad. (2021). **28**, 181–187



IUCr Journals

CRYSTALLOGRAPHY JOURNALS ONLINE

Copyright © International Union of Crystallography

Author(s) of this article may load this reprint on their own web site or institutional repository provided that this cover page is retained. Republication of this article or its storage in electronic databases other than as specified above is not permitted without prior permission in writing from the IUCr.

For further information see <https://journals.iucr.org/services/authorrights.html>

Submicronic Laue diffraction to determine in-depth strain in very closely matched complex HgCdTe/CdZnTe heterostructures with a 10^{-5} resolution

X. Biquard,^{a*} P. Ballet,^b A. Tuaz,^b P. H. Jouneau^a and F. Rieutord^a

^aUniversité Grenoble Alpes, CEA, IRIG, 38000 Grenoble, France, and ^bUniversité Grenoble Alpes, CEA, LETI, 38000 Grenoble, France. *Correspondence e-mail: xavier.biquard@cea.fr

Received 25 June 2020
Accepted 30 September 2020

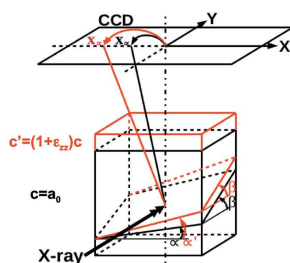
Edited by I. Schlichting, Max Planck Institute for Medical Research, Germany

Keywords: HgCdTe; Laue diffraction; high strain resolution; strain; microdiffraction; IR.

Cross-sectional submicronic Laue diffraction has been successfully applied to HgCdTe/CdZnTe heterostructures to provide accurate strain profiles from substrate to surface. Combined with chemical-sensitive techniques, this approach allows correlation of lattice-mismatch, interface compositional gradient and strain while isolating specific layer contributions which would otherwise be averaged using conventional X-ray diffraction. The submicronic spatial resolution allowed by the synchrotron white beam size is particularly suited to complex infrared detector designed structures such as dual-color detectors. The extreme strain resolution of 10^{-5} required for the very low lattice-mismatch system HgCdTe/CdZnTe is demonstrated.

1. Introduction

HgCdTe is today the material of choice for developing very high performance infrared (IR) detectors since its Hg/Cd ratio can be used to tune the band-gap, enabling short (SWIR) to mid (MWIR) and long wave (LWIR) selective IR band detection, thus covering a vast range of applications including telecoms, space investigation and astronomy. In particular, the very low band-gap HgCdTe alloy has led to high-performance devices with increased complexity, size, resolution, and operating temperature (Rothman *et al.*, 2009; Reibel *et al.*, 2011; Vilela *et al.*, 2013; Lee *et al.*, 2016). In IR detectors, HgCdTe layers are epitaxially grown on a CdZnTe substrate and, in principle, HgCdTe may be grown on a lattice-matched CdZnTe substrate. However, bulk crystals of CdZnTe present intrinsic Zn non-uniformities related to segregation during solidification (Brellier *et al.*, 2014), making perfect lattice matching impossible over large area wafers. Moreover, the introduction of molecular beam epitaxial (MBE) heterostructures, localized doping, dual-color detection or thermal annealing induces strong in-depth compositional gradients, as well as abrupt interfaces and multiple HgCdTe layers of different Hg/Cd ratio leading to layers that cannot be all matched to the substrate. Even though the lattice mismatch can be limited to very low 10^{-4} levels, efficient IR absorption requires a large thickness of HgCdTe which, combined with the low 10–20 MPa elastic limit of HgCdTe (Ballet *et al.*, 2013), may lead to misfit dislocation generation (Yoshikawa, 1988; Matthews & Blakeslee, 1974) and therefore to a rapid degradation of detector general performances (Jówickowski & Rogalski, 2000; Figgemeier *et al.*, 2003; Johnson *et al.*, 1992). Consequently, characterization of strain in those complex structures requires spatially resolved measurements to be meaningful.



While strain and plastic relaxation of a single epitaxial HgCdTe layer grown on a CdZnTe substrate have been studied through high-resolution X-ray diffraction (HRXRD) (Ballet *et al.*, 2013; Skauli & Colin, 2001), etch pit density revelation (Fourreau *et al.*, 2016) and surface cross-hatching observation (Tobin *et al.*, 1995; Martinka *et al.*, 2002), there has been no report of in-depth strain measurement. Here, we demonstrate that local diffraction using a submicronic white X-ray beam may provide a cross section of any HgCdTe/CdZnTe heterostructures with an in-depth spatial resolution of ~ 500 nm while still retaining the required resolution of 10^{-5} over the strain imposed by the very low lattice mismatch of the HgCdTe/CdZnTe system. This technique known as micro-Laue (Ice & Pang, 2009) is implemented on the BM32 beamline of the ESRF synchrotron (Ulrich *et al.*, 2011). It has been shown to successfully resolve localized strain fields induced by processing steps in HgCdTe photodiodes (Tuaz *et al.*, 2017) and is here used to measure in-depth strain profiles in three typical examples of MBE-grown heterostructures: a reference single epitaxial HgCdTe layer grown on a CdZnTe substrate, the same after thermal annealing, and the quite complex case of a dual-band detector that includes a Cd-rich barrier layer (Reibel *et al.*, 2011; Vilela *et al.*, 2013; Destefanis *et al.*, 2007).

2. Sample description

HgCdTe layers have been grown by MBE on $4\text{ cm} \times 4\text{ cm}$ (211)B CdZnTe substrates with a Zn fraction close to 4%. Hg, Cd and Te elements are provided by individual effusion cells while ZnTe sublimation is used to add Zn to the Cd-rich barrier layer in the dual-band detector sample. Constant fluxes are used for Hg and Te with a ratio close to 1000:1 to compensate for the strong Hg desorption at epitaxy temperature ($\sim 180^\circ\text{C}$), and the Cd flux is monitored to adjust for the nominal alloy composition profile during growth. Samples are cleaved along the (0, -1, 1) cleavage planes guaranteeing perpendicular cleaved surfaces, well suited for micro-Laue cross-section analysis. Three different samples of increasing complexity were studied to illustrate different material configurations:

(i) An as-grown sample made of a single epitaxial HgCdTe layer of constant alloy composition grown on a CdZnTe substrate, thus realizing an abrupt interface.

(ii) An annealed sample where the previous sample has undergone a strong thermal annealing under Hg-pressure, thus resulting in a graded substrate-layer interface.

(iii) Finally a dual-band detector sample which is a complete long-mid wave architecture that includes the two detection layers of HgCdTe with different alloy compositions, sandwiched between abrupt and graded interfaces including a Cd-rich barrier with a local addition of Zn to controllably stabilize the lattice constant during growth.

Composition profiles for these heterostructures have been obtained from secondary ion mass spectrometry (SIMS) depth profiling for as-grown and annealed samples and from scanning transmission electron microscope energy-dispersive

X-ray analysis (STEM-EDX) for the dual-band detector sample. In this case, the use of a TEM specimen thinned down to about 100 nm allows for a very good accuracy in the determination of both alloy composition and thickness of the layers, while SIMS generally suffers from cumulative uncertainties associated with variation of ion-beam etching speed with HgCdTe alloy composition (Wang *et al.*, 2007; Werner, 1994).

3. Data analysis

The micro-Laue setup implemented on the BM32 beamline at ESRF enables a white beam with all energies ranging from 5 to 23 keV to be focused down to a diameter of about 500 nm with diffraction peaks collected upwards with a CCD camera (Ulrich *et al.*, 2011). For this particular experiment, the sample is horizontally positioned with its growth direction vertical so that the cleaved cross-sectional plane is exactly perpendicular to the beam.

Strain is deduced from the position of the various diffraction peaks intercepted by the CCD camera. Generally speaking, the distance between sample and camera may be freely chosen as a shorter distance implies a less precise peak position determination compensated by a larger number of peaks, while a longer one lowers the number of peaks but increases the precision of the position determination. In our case, peaks are angularly very sharp and the same stands for the point spread function of the CCD (~ 1.2 pixels). Therefore, for low distances, peak intensity will be focused into a single or two pixels which has two main consequences. Firstly, as peak position determination takes into account a certain number of pixels neighboring the local maxima, it will be influenced by quite a lot of low signal-to-noise ratio pixels: this will highly degrade the precision of the peak position determination, a phenomenon that may not be fully compensated by the increase in peak number. Secondly, the peak shape is fairly asymmetrical along both X and Y but will wrongly appear as much more symmetrical if the distance is too close. Therefore, the peak position found when using symmetrical fit as in both reference micro-Laue programs *XMAS* (Tamura, 2014) and *LaueTools* (Micha, 2020) will suffer from a systematical error whose value varies with the peak considered as well as its asymmetrical component proportion. To avoid both phenomenons, our criterion was that the peak intensity distribution full width at half-maximum (FWHM) must be larger than 3 pixels and the camera was placed sufficiently far away to meet this criterion. The reference micro-Laue program *XMAS* was only used here to determine Bragg peak indexes and their approximate energies; and, since the peak intensity distribution is fairly asymmetrical along both X and Y , we developed our own data analysis procedure.

The first step consists of a careful background evaluation in order to differentiate between a varying background and the asymmetrical peak shape. Image is processed as a whole using the iterative Brückner algorithm that robustly removes any smooth varying components as background for 1D 2θ XRD

scans (Brückner, 2000). It was generalized in 2D by applying it successively on X and Y lines. After these two passes, we keep for each pixel background value the minimum of the two values found, and we stop iteration when the maximum intensity correction of an iteration drops below 1. Overall, this step spectacularly reduces the average background level of collected images on our 16-bit Mar-165 CCD camera typically from the range 30–120 down to 3–8.

The second step consists of a peak selection as a function of their energies, energies being roughly estimated thanks to their indexes. Since the incoming X-ray beam cut-off energy on BM32 is 23 keV (Ulrich *et al.*, 2011), among all intercepted diffraction peaks we select those that are of a sufficiently high energy (> 12 keV) to make sure they do not contain harmonics in order to prevent enlargement. Indeed, dynamical diffraction theory (Als-Nielsen & McMorro, 2011) shows that, in contrast to Bragg's law, harmonics are not perfectly superimposed on the fundamental since harmonics have lower Darwin width and also a lower offset to the Bragg angle (both proportional to the inverse of the order). Note that in monochromatic beam mode, this angular difference can be used to enhance the monochromator's harmonics rejection by a slight angular detuning (Schulte-Schrepping & Drube, 2001). This procedure selects 10 out of the 20 collected diffraction peaks, still enough for strain measurement. The selected 12–23 keV energy range corresponds to an X-ray penetration length range of 20–120 μm in the substrate and 15–40 μm in the layer: the X-ray diffraction probes the inside of our sample, not just the exterior plane of the cleaved surface which probably undergoes free surface relaxation effects.

The third step consists of measuring selected peak positions. To that end, we developed our own fitting program which independently takes into account the X and Y peak shape to measure peak positions. Diffraction peaks are found to be larger along X than Y , so that 9 and 7 successive intensity profiles are taken along X and Y for each peak. Since the strain is low, the peak position does not vary by more than ± 2 pixels during an X-ray beam scan: for each diffraction peak, we consider the same X and Y profiles whatever the X-ray beam position, thus minimizing the effect of any residual geometrical aberrations of the CCD. For each intensity profile, we adjust two independent pseudo-Voigt (PV) functions and a small residual background level. Once fitted, we calculate the central position for each intensity profile as their center of mass while the final peak position is taken as the average of these central positions weighted by the total intensity of each profile.

Cross-section line profiling consists of recording successive CCD images at different heights relative to the substrate/layer interface. As our samples are made of epitaxially deposited layers with low mismatch ($< 3 \times 10^{-4}$), and, because it has been experimentally shown in this particular system that in-plane strain anisotropy is limited to the compressive case and with only minor contribution (Ballet *et al.*, 2013), we will assume the strain to be bi-axial. Moreover, as the substrate is far more rigid than HgCdTe layers and because of our low lattice mismatch, the substrate remains unstrained sufficiently

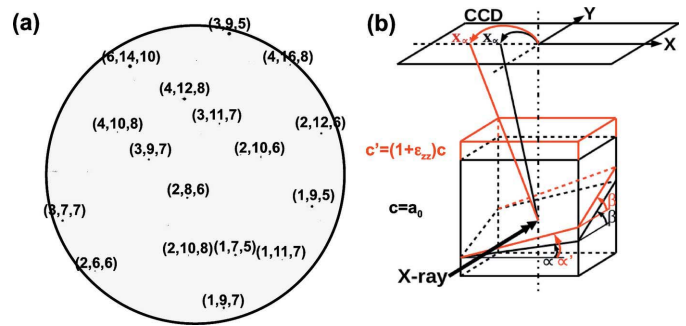


Figure 1
(a) Distribution of the diffracted peaks intercepting the CCD camera together with their Bragg indexes using the CdTe unit cell. (b) Schematic showing how bi-axial strain ϵ_{zz} changes the X component X_α of the unstrained (in black) peak position into the strained (in red) X component $X_{\alpha'} = (1 + \epsilon_{zz})X_\alpha$ since it induces a diffraction plane rotation $\alpha \rightarrow \alpha' = (1 + \epsilon_{zz})\alpha$ in the (X, Z) plane.

far away from the interface. About 5 μm would be enough, but, to be consistent with previous study (Tuaz *et al.*, 2017), we took as an unstrained reference the measurement at 50 μm underneath the interface.

The scheme in Fig. 1(b) illustrates how peak positions are modified with strain and shows that the peak position displacement from its unstrained reference position (written as peak displacement hereafter) is directly linked to the out-of-plane deformation component $\epsilon_{zz} = (c' - c)/c$. Therefore, as in the laboratory diffraction case, measuring the peak displacement of any single peak is enough to determine ϵ_{zz} . Nevertheless, to maximize precision, we will naturally take advantage of our simultaneous measurements of multiple diffraction peaks and the straightforward idea is to take the average over all peak displacements. But the average of all peak displacements is sensitive to (even slight) variations of local orientation, should it originate from layer growth tilt, scanning translation wobble, X-ray beam angular stability, *etc.* It is also sensitive to any variation of the position of the origin point of the CCD — located at the exact vertical of the X-ray beam impact on the sample's cleaved surface, should it come from surface non-flatness, perpendicular misalignment, *etc.* To avoid all these sources of measurement errors, rather than simply averaging peak displacements, we shall use their relative movements.

Indeed, it is obvious that $X_{\alpha'} = (1 + \epsilon_{zz})X_\alpha$ [refer to Fig. 1(b)] if peak angles relative to Z stay small. Here peak angles are limited to 0.26 rad (15°) and, moreover, the range of validity of this equality is fairly extended since it remains valid when using Taylor series expansions of trigonometric tan and arctan functions until order 4. Consequently, the peak displacement along X , *i.e.* $X_{\alpha'} - X_\alpha$, correlates linearly with unstrained reference peak X position X_α as illustrated in Fig. 2 for three different depths (b), (c) and (d) in the cross-section line profile (a). In fact, the scheme of Fig. 1(b) may be drawn in any plane including the Z axis, so that displacements may be indifferently measured along X , Y or any linear combination of X and Y . However, along Y , peak positions

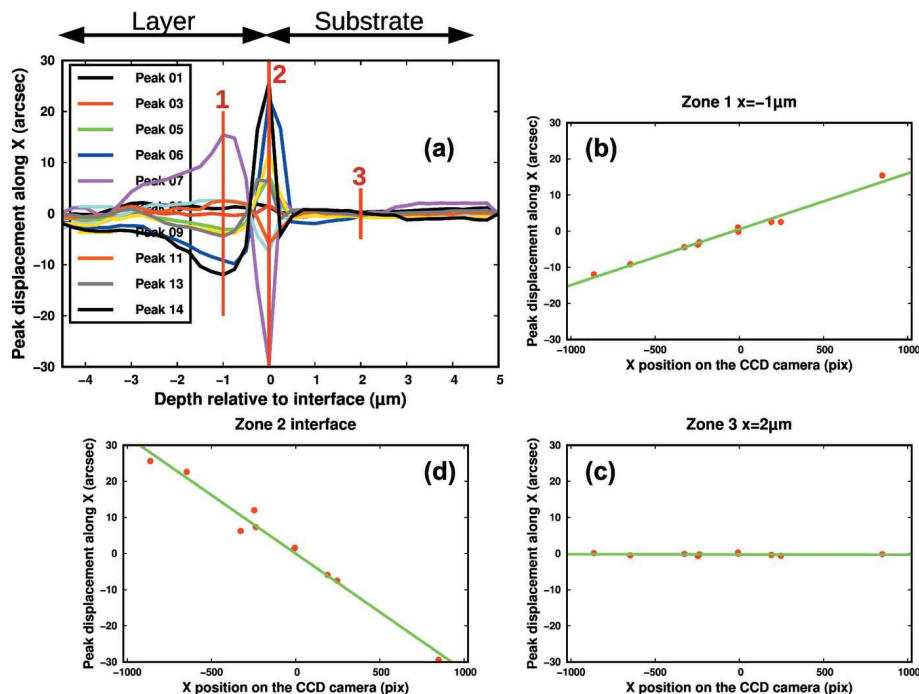


Figure 2
For the annealed sample, panel (a) shows selected peak displacements along X as a function of depth relative to the layer/substrate interface, the reference being placed $50\ \mu\text{m}$ deep into the CdZnTe substrate. Panels (b), (c) and (d) are plots of peak displacement as a function of their position on the camera for the three zones marked as 1, 2 and 3 in (a) and, corresponding to the HgCdTe layer, the layer/substrate interface and the CdZnTe substrate, respectively.

depend on the X-ray beam penetration length which varies with peak energy whereas this effect does not exist along X , thus explaining why the displacement along X was preferred.

Finally, the fourth step consists of the linear regression of peak displacements along X as a function of their unstrained X position. The absolute local strain value ϵ_{zz} is simply obtained as the slope while the intercept is equal to (the tangent of) two times the local orientation in the (X, Z) plane. We thus determine both the evolution of the local strain and orientation with depth for any cross section. In Fig. 1, the CCD camera is considered to be perfectly parallel to the incoming X-ray beam direction: any roll [any yaw] of the CCD camera relative to the beam direction will lead to a small over-estimation [underestimation] of both peak position and displacement. Therefore, as slope is their ratio, these angles have a minor influence. Moreover, using the $50\ \mu\text{m}$ deep unstrained reference point, we were able to estimate these angles, both being found inferior to 1° and therefore their influence on slope may be neglected.

In contrast with classical microdiffraction Laue experiments, our method does not require a dedicated calibration step to finely determine the position of the CCD camera relative to the incoming X-ray beam to be conducted. This usually requires a large sample holder movement (typically in the centimetre range) to substitute the sample with a strain-free reference sample. Our method only requires a means to select harmonic-free diffraction peaks: a rough camera positioning is sufficient here. No reference sample is used, thus preventing our results from being tainted by both CCD

camera positioning uncertainties as well as large sample holder movement induced positioning errors.

4. Results

4.1. As-grown sample

Fig. 3(a) shows the chemical profile obtained by SIMS for Cd (in black) and Zn (in blue) on a $4.5\ \mu\text{m}$ -thick MBE-grown HgCdTe/CdZnTe abrupt structure: Cd and Zn fractions are logically found to be constant both inside the whole substrate and the whole layer. Fig. 3(b) shows the extracted strain (in red) as a function of depth, the Hg-fluorescence (in green) being recorded simultaneously. Since the sample is as-grown, ideally the Hg-fluorescence should be a step-down function marking the layer/substrate interface with a 100% value inside the layer and a zero value inside substrate. On the surface side, there is an apparent drop in Hg concentration: in fact, this originates from part of the beam simply passing above the sample. On the substrate side,

a non-zero Hg-fluorescence value is measured: indeed, when the X-ray beam probes the substrate, this will generate sufficiently energetic diffracted beams directed towards the above HgCdTe layer, thus inducing Hg-fluorescence in it. Taking this

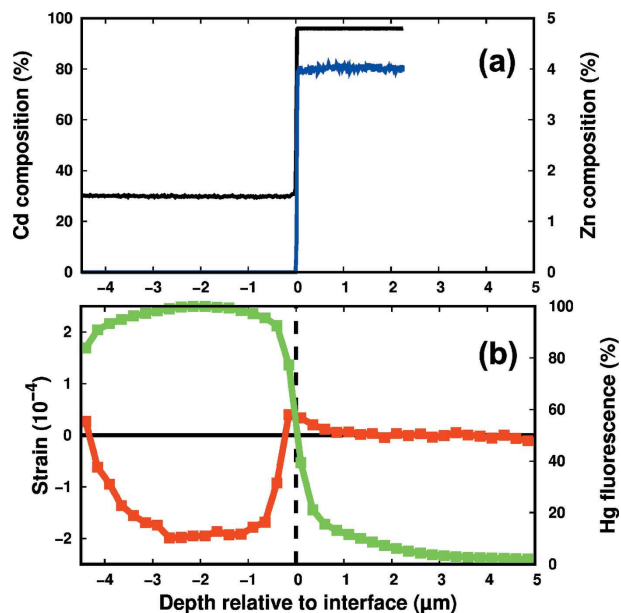


Figure 3
As-grown sample made of a $4.5\ \mu\text{m}$ -thick MBE-grown HgCdTe/CdZnTe abrupt structure. (a) SIMS profiles with respective cadmium (black, left scale) and zinc (blue, right scale) fraction. (b) Micro-Laue measurements with Hg fluorescence (green, right scale) and micro-diffraction derived strain (red, left scale).

effect into account, the beam shape could be deduced from the transition at the layer/substrate interface: the beam shape was very well fitted using a PV function including 20% Lorentzian with a beam FWHM of 580 nm. Strain shows a spectacular increase starting at the interface and goes from a constant 0 in the substrate to another constant -2×10^{-4} in the first 2.5 μm of the layer, this transition occurring on a ~ 600 nm depth reflecting the beam FWHM. This strain plateau is followed by a rather slow decrease of the strain until reaching zero again when reaching the free surface. This clearly shows that the substrate is indeed free of strain, and that the layer experiences some relaxation of the strain after a critical ~ 2.5 μm thickness. The demonstration of the inhomogeneous nature of the strain over layer thickness, possibly associated with misfit dislocation generation after 2.5 μm of growth, clearly points to the benefit of micro-Laue cross section compared with conventional X-ray diffraction techniques.

4.2. Annealed sample

In order to further illustrate the ability of micro-Laue scattering to resolve non-uniform strain profiles, another sample was processed out of the same HgCdTe/CdZnTe wafer used for the previous sample. This sample was annealed for several hours at elevated temperature, resulting in a significant interface intermixing between Hg, Cd and Zn as is clearly observed on the SIMS profiles of Fig. 4(a). The sample presents a $3 \pm 0.5 \times 10^{-4}$ mismatch between layer and substrate as measured by HRXRD, and Fig. 4(b) shows the strain evolution with depth in red, and presents many interesting features.

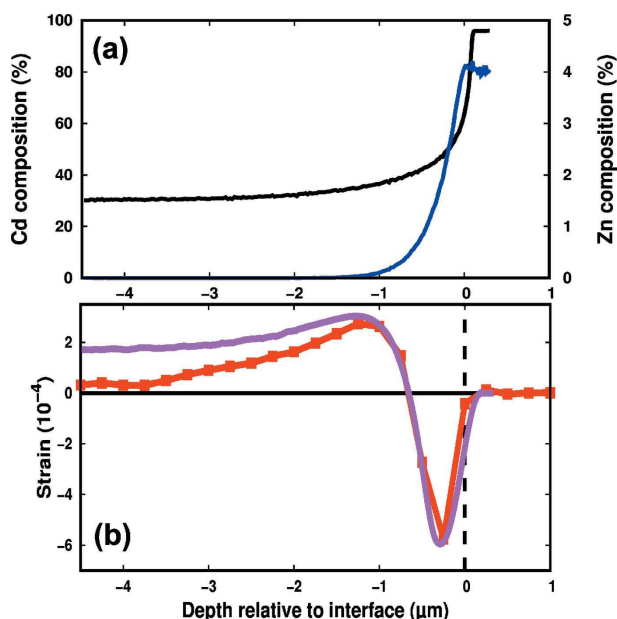


Figure 4 Annealed sample made of the 4.5 μm -thick MBE-grown HgCdTe/CdZnTe abrupt structure of the as-grown wafer after annealing. (a) SIMS profiles with respective cadmium (black, left scale) and zinc (blue, right scale) fraction. (b) Strain derived from micro-Laue measurements in red and the calculated bi-axial strain in magenta using SIMS data in (a) for HgCdZnTe to evaluate the local lattice parameter.

Firstly, in the substrate zone (positive depth), we expect a constant and null strain. Indeed, we find a $1.1 \pm 1.3 \times 10^{-5}$ strain, thus confirming the absence of strain inside the substrate and demonstrating a strain measurement sensitivity of $\pm 1.3 \times 10^{-5}$, a sensitivity that matches the state-of-the-art Bragg diffraction coherent imaging performances (Chahine *et al.*, 2014). Secondly, with a positive $3 \pm 0.5 \times 10^{-4}$ mismatch, we would expect a positive constant strain inside the layer: the most spectacular feature is this unexpected huge negative strain found right on the interface! Clearly a dedicated effect occurs specifically at the interface leading to a huge contraction of the *c*-axis while strain becomes positive again once outside this ~ 1 μm -thick interface zone. Moreover, this negative strain is way too high compared with the elastic limit of HgCdTe ($\sim 3 \times 10^{-4}$) but could be easily supported by CdZnTe. This spectacular effect was caused by the 5 h thermal annealing of the sample: it has induced an Hg exo-diffusion from layer to substrate and reciprocally the exo-diffusion of Zn and Cd from the substrate inside the layer, creating a quaternary HgCdZnTe interface. Despite the Zn fraction in the substrate being low (about 4%), the much smaller lattice parameter of ZnTe (Bhunia & Bose, 1998) compared with CdTe or HgTe (Skauli & Colin, 2001) implies that even a small fraction of Zn inside the HgCdTe layer will induce an important variation of the local lattice constant which may be simulated using the SIMS profiles of Fig. 4(a). The corresponding bi-axial strain evolution is represented in magenta in Fig. 4(b): there is a remarkable matching through the interface until 1 μm inside the layer between strain values expected from local composition and measured with micro-Laue (SIMS depth precision is 10 nm, data were convoluted with a 580 nm PV to match the X-ray beam size). Therefore, the huge negative strain found at the interface comes from the compositional gradient induced by thermal annealing. Beyond this compositional gradient, strain is much smaller, goes down to zero and remains zero 3.5 μm after the interface. As for the as-grown sample, strain relaxation mechanisms appear to take place after a critical ~ 1 μm thickness, reducing the net strain from 2.5×10^{-4} to zero in a thickness of about 2.5 μm . Even though the current measurement does not provide clear proof of extended defect generation in this slab of material (no significant peak shape evolution or peak broadening were found), dislocation generation seems the most probable mechanism underway. And the very low density of misfit dislocations needed to accommodate such a weak mismatch makes the absence of any specific peak shape evolution understandable. Of course, our bi-axial hypothesis does not stand beyond the critical thickness. Therefore, for the 1 μm -thick HgCdTe slab situated at the surface where we measure a zero strain, this does not mean that this slab of the layer is lattice-matched to the substrate but rather that it is not strained by the substrate.

4.3. Dual-band detector

Dual-band detector stacks used for simultaneous detection of two IR bands represent one of the most advanced design in

HgCdTe technology. It combines two photodiodes, each made of an absorbing layer of specific Hg/Cd ratio and thickness for selective IR band detection, and a Cd-rich barrier to prevent electrical crosstalk between the two photodiodes. Band-gap engineering is used for the individual design of each photodiode and usually consist of higher band-gap thin layers and composition graded interfaces. The specimen of interest here is a superposition of MWIR and LWIR absorbing layers deposited onto a substrate whose Zn content was chosen to match the LWIR layer.

The sample's Cd, Zn and Hg composition profiles were measured using STEM-EDX as shown in Fig. 5(a), which was performed on a thinned lamella of less than 100 nm thickness, thus preventing resolution degradation coming from lateral diffusion/interaction with the electron beam. The whole stack is 11 μm thick and consists, after the CdZnTe substrate, of first a 6.3 μm -thick MWIR absorbing layer with a 30% Cd composition (which starts with a 0.7 μm -thick ramp-down of Cd composition from 40% to 30%), separated from the second 2.3 μm -thick LWIR absorbing layer by a Cd-rich barrier. This barrier is made of two symmetrical 0.3 μm -thick graded interfaces around a 0.7 μm -thick plateau at 80% Cd composition. The second absorbing LWIR layer is set for a 80 K cut-off wavelength of 9.5 μm corresponding to a Cd composition of 22%. The stack is terminated by a capping heterostructure containing a short 0.2 μm -thick ramp-up from the LWIR to the MWIR composition, a 0.55 μm -thick MWIR plateau and finally a 0.35 μm -thick gap-opening layer made with a ramp-up until 100% Cd composition for surface passivation. ZnTe is added to the Cd-rich barrier and the gap-opening layer to prevent too-large deviation from lattice matching conditions in order to keep the defect density at a level compatible with high-performance devices.

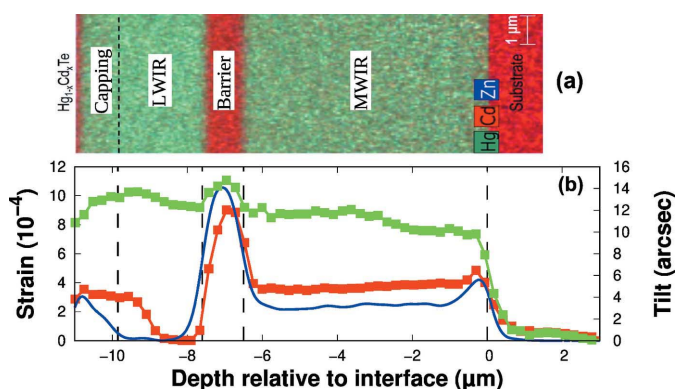


Figure 5

The STEM-EDX results obtained on the dual-band sample are shown in (a) with Hg, Cd and Zn local concentration represented in green, red and blue. The five zones of the sample are perfectly visible: the substrate and its abrupt interface with the MWIR layer of constant composition, the barrier with both its graded interface, the lattice-matched LWIR layer of constant composition and its transition to the capping layer whose composition varies continuously from low to high Cd content. In (b), the red and green curves represent the micro-diffraction derived strain and tilt, respectively, while the blue curve shows results of the calculation of the strain using STEM-EDX data to evaluate the local HgCdZnTe lattice parameter. Note that the colors in (a) and (b) do not represent the same values.

Cross-scanning of this complex heterostructure resulted in the plot in Fig. 5(b) where the measured strain (red curve) is given as a function of depth and compared with the calculated bi-axial strain (blue curve) which uses the local quaternary lattice constant deduced from STEM-EDX chemical profiles (STEM-EDX depth precision is 15 nm, data were convoluted with a 580 nm PV to match the X-ray beam size). The two curves look much alike with close transition positions and similar intensity profiles. Nevertheless, some important differences remain, especially when considering strain intensity distribution inside layers.

As with our two previous examples, deep inside the substrate, measured and calculated strains are zero as expected for any non-deformed bulk material. Considering Fig. 5(b) from substrate (right) to surface (left), we observe that both measured and calculated strains logically show a clear step-up at the HgCdTe/CdZnTe interface. This step-up is followed by a constant plateau throughout the full MWIR layer thickness indicating a homogeneous lattice deformation. It is preceded by an over-intensity that corresponds to the ramp-down of Cd composition from 40% to 30%. We clearly observe that the measured strain is 50% more intense than the calculated one. If there was no further layer, as is the case for the as-grown sample [see Fig. 3(b)], we should expect the measured strain inside the MWIR layer to closely follow the calculated one. Therefore, it is likely that the very high strain found inside the barrier was distributed to the MWIR layer, thus raising its strain by 50% while decreasing the measured barrier strain by 20% compared with the calculated one. And this strain distribution phenomenon even extends until the rigid substrate, thus explaining the slight decreasing strain from the interface down to 3 μm in the substrate.

Above the high strained barrier, we find the LWIR layer whose first half is perfectly relaxed with an extremely low residual strain of 0.2×10^{-5} , an expected result since the LWIR layer was set to be lattice matched to the substrate. Calculated and measured strains then clearly split apart in the second half of the LWIR layer, through the capping heterostructure until they match again in the gap-opening layer. This layer being 1.5 times thinner than the beam size, convolution with the beam size to allow comparison with measured strain has considerably smoothed out its maximum: in fact, the gap-opening layer experiences a large average strain of 7.5×10^{-4} . Therefore, the gap-opening layer is highly strained and the same phenomenon of strain distribution occurs, raising the strain inside the capping heterostructure as well as half the LWIR layer.

Overall, the strain is compressive in all layers except in the LWIR layer for which it falls to zero as a result of lattice matching with CdZnTe. The addition of Zn in the barrier layer is clearly not sufficient to keep the lattice parameter constant but is large enough to prevent lattice relaxation. Indeed, a too large Zn fraction in the barrier would result in a strain inversion to the tensile side, thus making strain balancing difficult to implement since strain relaxation occurs at a two time smaller mismatch for tensile than compressive HgCdTe (Ballet *et al.*, 2013).

Finally, local orientation is shown as the green curve of Fig. 5(b). It logically stays constant in the substrate zone and presents a marked step-up at the interface position while staying roughly constant in the interval 8–11 arcsec throughout the whole layer stacks. This indicates that the first layer presents a reasonable growth plane tilt of 8 ± 1 arcsec while all successive planes were grown without any noticeable further disorientation. With an estimated 1 arcsec resolution in orientation, micro-Laue shows a remarkable resolution compared with HRXRD where, in the best case of single HgCdTe layer, diffraction peaks display a 10–15 arcsec FWHM.

5. Conclusion

This last dual-band detector sample clearly shows the ability of the micro-diffraction technique to provide fully quantitative profiles of both strain and orientation relative to the substrate in complex heterostructure of otherwise very closely matched materials. This arises thanks to the spatial resolution (~ 500 nm) but also to the high sensitivity in diffraction peak position determination leading to a remarkable 10^{-5} resolution in local strain measurement as well as 1 arcsec resolution in local orientation determination. As a comparison, extensively used conventional HRXRD fails in effectively separating the different layer contributions because of too close diffraction peaks but also because of the attenuation/absorption lengths in these heavy materials preventing accurate in-depth information to be extracted. Also, the use of electron microscopy diffraction techniques has been proved to be practically unable to provide strain information over such in-depth range: samples prepared for such techniques with a field of analysis larger than a few micrometres strongly suffer from thickness non-uniformity and lamella thinning strain relieving effects. Micro-Laue really appears as a reference high-definition characterization tool perfectly suited to study the local strain and plane orientation profiles inside any kind of closely matched multilayer deposited on a substrate.

References

- Als-Nielsen, J. & McMorrow, D. (2011). *Elements of Modern X-ray Physics*, 2nd ed. New York: John Wiley & Sons.
- Ballet, P., Baudry, X., Polge, B., Brellier, D., Merlin, J. & Gergaud, P. (2013). *J. Elec Mater.* **42**, 3133–3137.
- Bhunia, S. & Bose, D. N. (1998). *J. Cryst. Growth*, **186**, 535–542.
- Brellier, D., Gout, E., Gaude, G., Pelenc, D., Ballet, P., Miguët, T. & Manzato, M. C. (2014). *J. Elec Mater.* **43**, 2901–2907.
- Brückner, S. (2000). *J. Appl. Cryst.* **33**, 977–979.
- Chahine, G. A., Richard, M.-I., Homs-Regojo, R. A., Tran-Caliste, T. N., Carbone, D., Jacques, V. L. R., Grifone, R., Boesecke, P., Katzer, J., Costina, I., Djazouli, H., Schroeder, T. & Schilli, T. U. (2014). *J. Appl. Cryst.* **47**, 762–769.
- Destefanis, G., Baylet, J., Ballet, P., Castelein, P., Rothan, F., Gravrand, O., Rothman, J., Chamonal, J. P. & Million, A. (2007). *J. Elec Mater.* **36**, 1031–1044.
- Figgemeier, H., Bruder, M., Mahlein, K.-M., Wollrab, R. & Ziegler, J. (2003). *J. Elec Mater.* **32**, 588–591.
- Fourreau, Y., Pantzas, K., Patriarche, G. & Destefanis, V. (2016). *J. Elec Mater.* **45**, 4518–4523.
- Ice, G. E. & Pang, J. W. L. (2009). *Mater. Charact.* **60**, 1191–1201.
- Johnson, S. M., Rhiger, D. R., Rosbeck, J. P., Peterson, J. M., Taylor, S. M. & Boyd, M. E. (1992). *J. Vac. Sci. Technol. B*, **10**, 1499–1506.
- Jówikowski, K. & Rogalski, A. (2000). *J. Elec Mater.* **29**, 736–741.
- Lee, D., Carmody, M., Piquette, E., Dreiske, P., Chen, A., Yulius, A., Edwall, D., Bhargava, S., Zandian, M. & Tennant, W. E. (2016). *J. Elec Mater.* **45**, 4587–4595.
- Martinka, M., Almeida, L. A., Benson, J. D. & Dinan, J. H. (2002). *J. Elec Mater.* **31**, 732–737.
- Matthews, J. W. & Blakeslee, A. E. (1974). *J. Cryst. Growth*, **27**, 118–125.
- Micha, J.-S. (2020). *LaueTools*, <https://gitlab.esrf.fr/micha/lauetools>.
- Reibel, Y., Chabuel, F., Vaz, C., Billon-Lanfrey, D., Baylet, J., Gravrand, O., Ballet, P. & Destefanis, G. (2011). *Proc. SPIE*, **8012**, 801238.
- Rothman, J., Baier, N., Ballet, P., Mollard, L., Fournier, M., Gout, J. S. & Chamonal, J.-P. (2009). *J. Elec Mater.* **38**, 1707–1716.
- Schulte-Schrepping, H. & Drube, W. (2001). *Nucl. Instrum. Methods Phys. Res. A*, **467–468**, 396–399.
- Skauli, T. & Colin, T. (2001). *J. Cryst. Growth*, **222**, 719–725.
- Tamura, N. (2014). *Strain and Dislocation Gradients from Diffraction*, pp. 125–155. London: Imperial College Press.
- Tobin, S. P., Smith, F. T. J., Norton, P. W., Wu, J., Dudley, M., Marzio, D. D. & Casagrande, L. G. (1995). *J. Electron. Mater.* **24**, 1189–1199.
- Tuaz, A., Ballet, P., Biquard, X. & Rieutord, F. (2017). *J. Elec Mater.* **46**, 5442–5447.
- Ulrich, O., Biquard, X., Bleuet, P., Geaymond, O., Gergaud, P., Micha, J. S., Robach, O. & Rieutord, F. (2011). *Rev. Sci. Instrum.* **82**, 033908.
- Vilela, M. F., Olsson, K. R., Norton, E. M., Peterson, J. M., Rybnicek, K., Rhiger, D. R., Fulk, C. W., Bangs, J. W., Lofgreen, D. D. & Johnson, S. M. (2013). *J. Elec Mater.* **42**, 3231–3238.
- Wang, L., Wang, A. & Price, S. (2007). *J. Elec Mater.* **36**, 910–912.
- Werner, H. (1994). *Mikrochim. Acta*, **114–115**, 107–127.
- Yoshikawa, M. (1988). *J. Appl. Phys.* **63**, 1533–1540.